nature physics

Article

https://doi.org/10.1038/s41567-023-02279-x

Ultrafast formation of topological defects in a two-dimensional charge density wave

Received: 17 November 2022

Accepted: 4 October 2023

Published online: 4 January 2024

Check for updates

Yun Cheng[1,2,12], Alfred Zong[3,4,12] ✉, Lijun Wu[5], Qingping Meng[5], Wei Xia[6,7], Fengfeng Qi[1,2], Pengfei Zhu[1,2], Xiao Zou[1,2], Tao Jiang[1,2], Yanfeng Guo[6], Jasper van Wezel[8], Anshul Kogar[9], Michael W. Zuerch[3,4] ✉, Jie Zhang[1,2,10] ✉, Yimei Zhu[5] ✉ & Dao Xiang[1,2,10,11] ✉

Topological defects play a central role in dynamical systems undergoing a non-adiabatic transition. In solids, topological defects as a result of femtosecond laser excitation have attracted increasing interest not only because they are key to understanding phase transitions but also because they can generate a variety of hidden orders that are not accessible in thermal equilibrium. Despite the common occurrence of these defects in a non-equilibrium system, the fundamental limit on how fast they can emerge in solids and the generic pathway for defect creation at such fast timescales have remained open questions. Here we apply ultrafast electron diffraction to study the reciprocal-space signatures of transient defects in a two-dimensional charge density wave, where simultaneous measurements of both defect and phonon dynamics yield a microscopic view of defect formation in the femtosecond regime. We find that one-dimensional domain walls are generated well within 1 ps following photoexcitation, during which the defect growth is not dictated by the amplitude of the order parameter, but is mediated by a non-thermal population of longitudinal optical phonons. Our work provides a framework for the ultrafast engineering of topological defects that are coupled to specific collective modes, which will prove useful for the dynamical control of non-equilibrium phases in correlated materials.

An important pathway to realize emergent states out of equilibrium is via the creation of topological defects. These singularities not only modify the local amplitude and phase of the underlying order parameter but they also change the elementary excitations of a symmetry-broken state[1,2]. In strongly correlated materials, photoinduced defects have been shown to correlate with a bandgap opening near the Fermi level[3] and insulator–metal transitions[4,5]. In systems that host several proximal states of matter, these defects can further seed the transient growth

[1]Key Laboratory for Laser Plasmas (Ministry of Education), School of Physics and Astronomy, Shanghai Jiao Tong University, Shanghai, China. [2]Collaborative Innovation Center of IFSA (CICIFSA), Shanghai Jiao Tong University, Shanghai, China. [3]Department of Chemistry, University of California at Berkeley, Berkeley, CA, USA. [4]Materials Sciences Division, Lawrence Berkeley National Laboratory, Berkeley, CA, USA. [5]Condensed Matter Physics and Materials Science Division, Brookhaven National Laboratory, Upton, NY, USA. [6]School of Physical Science and Technology, ShanghaiTech University, Shanghai, China. [7]ShanghaiTech Laboratory for Topological Physics, Shanghai, China. [8]Institute for Theoretical Physics Amsterdam, University of Amsterdam, Amsterdam, the Netherlands. [9]Department of Physics and Astronomy, University of California at Los Angeles, Los Angeles, CA, USA. [10]Tsung-Dao Lee Institute, Shanghai Jiao Tong University, Shanghai, China. [11]Zhangjiang Institute for Advanced Study, Shanghai Jiao Tong University, Shanghai, China. [12]These authors contributed equally: Yun Cheng, Alfred Zong. ✉e-mail: alfredz@berkeley.edu; mwz@berkeley.edu; jzhang1@sjtu.edu.cn; zhu@bnl.gov; dxiang@sjtu.edu.cn

https://doi.org/10.1038/s41567-023-02279-x

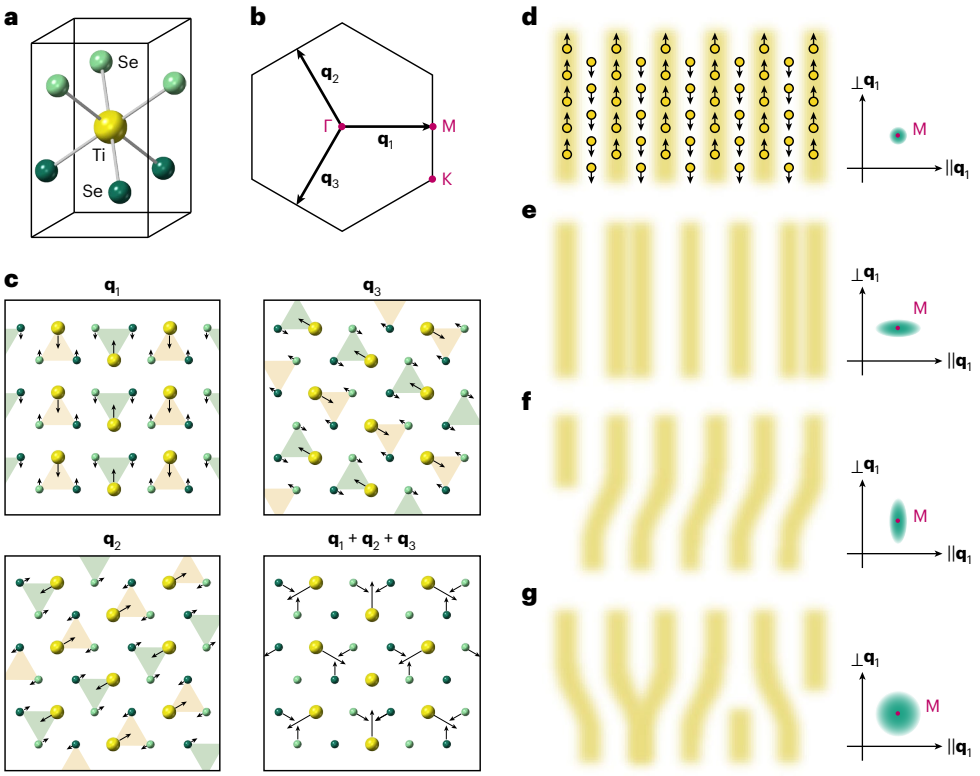

Fig. 1 | 2 × 2 CDW in 1T-$TiSe_2$ and possible types of topological defect in the CDW. a, Crystal unit cell of 1T-$TiSe_2$ in the non-CDW state, where each Ti atom is octahedrally coordinated with six Se atoms. The upper and lower Se atoms are differently coloured. **b**, Projected Brillouin zone of the non-CDW state with high-symmetry points labelled. The arrows indicate the three wavevectors of the short-range 2 × 2 CDW, which exists right above the transition temperature of the long-range 2 × 2 × 2 CDW order. **c**, Top view of the crystal structure, where CDW-induced atomic displacements in a single layer are labelled by the arrows for the indicated wavevector ($\mathbf{q}_1$ to $\mathbf{q}_3$). For visual clarity, the length of the displacement vectors and the ratio between Ti and Se displacements are not drawn to scale. The green and beige triangles highlight alternating chains of anti-phase displacements in each wavevector. **d**–**g**, Schematic of different topological defects in the 2 × 2 CDW for wavevector $\mathbf{q}_1$ (left) and the corresponding superlattice peak shape at the M point imaged in a 2D detector (right). Panel **d** shows the state free from defects, where only Ti displacements are drawn. The yellow and white stripes correspond to CDW displacement chains with opposite phases. Possible topological defects include 1D domain walls (**e**), shear (**f**) and dislocations (**g**).

of a competing phase that is normally hidden in equilibrium[6]. Despite the ubiquity of non-equilibrium topological defects, their ephemeral nature makes it challenging to obtain a precise characterization of their evolution in space and time. Although the dynamics of defect annihilation are well studied as they take place over a few picoseconds to several minutes[7–11], it remains unclear how individual defects are formed in the first place and what limits the timescale of defect generation in the femtosecond regime.

Two-dimensional (2D) materials have been of great interest in the investigation of defect dynamics since pioneering studies were conducted on 2D liquid crystals[12–14]. At equilibrium, topological defects readily appear due to pronounced thermal fluctuations in reduced dimensions, giving rise to exotic phases involving nematic, tetratic or hexatic orders depending on the underlying crystal symmetry[15,16]. Although scanning microscopes can image individual defects down to the atomic scale[17–19], the dynamics of nanoscopic defects are often too fast to capture with traditional probes. To understand the mechanism of defect formation at the femtosecond timescale, we use an ultrashort light pulse to create topological defects in a 2D charge density wave (CDW), and we examine their temporal evolution encoded in diffuse scattering in momentum space[20]. Unlike specular peaks, the diffuse intensity is orders-of-magnitude smaller, rendering quantitative analysis difficult. We developed a femtosecond megaelectronvolt (MeV) electron diffraction beamline, whose high electron flux enabled an ultrasensitive probe of diffuse signals without compromising the temporal resolution[21] (Methods and Supplementary Note 1). From the same set of diffraction images, we were able to simultaneously record branch-specific phonon dynamics[22] as topological defects were formed. The concurrent detection of both topological defects and non-thermal phonons offers a striking visualization of different stages in defect growth, providing an unprecedented view on the mechanism of ultrafast defect generation in a broken-symmetry state.

Our material choice is a layered transition metal dichalcogenide, 1T-$TiSe_2$ (Fig. 1a), which forms a 2 × 2 × 2 commensurate CDW below $T_c \approx 195$ K. In each layer, the density modulation is a superposition of three symmetry-equivalent wavevectors $\mathbf{q}_1$ to $\mathbf{q}_3$ (Fig. 1b,c), whose associated atomic displacements in adjacent layers are out of phase by exactly π. Right above T_c, photoemission and diffraction measurements reveal a 2D version of the ground-state CDW[23,24], featuring short-range 2 × 2 superlattices in individual layers that are largely uncoupled between layers. The existence of this 2D CDW allows us to explore defect dynamics in a reduced dimension without resorting to an atomically thin crystal.

Although an unambiguous determination of topological defects is best resolved in microscopy measurements in real space, the type of CDW defects can also be deduced in diffraction experiments by studying the spatial profile of the superlattice peak. Focusing on a particular wavevector, such as $\mathbf{q}_1$, we expect a δ-function-like peak at the M point if no defects are present, corresponding to perfect atomic displacements that form anti-phase chains running perpendicular to $\mathbf{q}_1$ (Fig. 1d). If defects are present, the δ peak gains a finite width, whose anisotropy is indicative of the defect structure. In the context of a stripe-like CDW,

https://doi.org/10.1038/s41567-023-02279-x

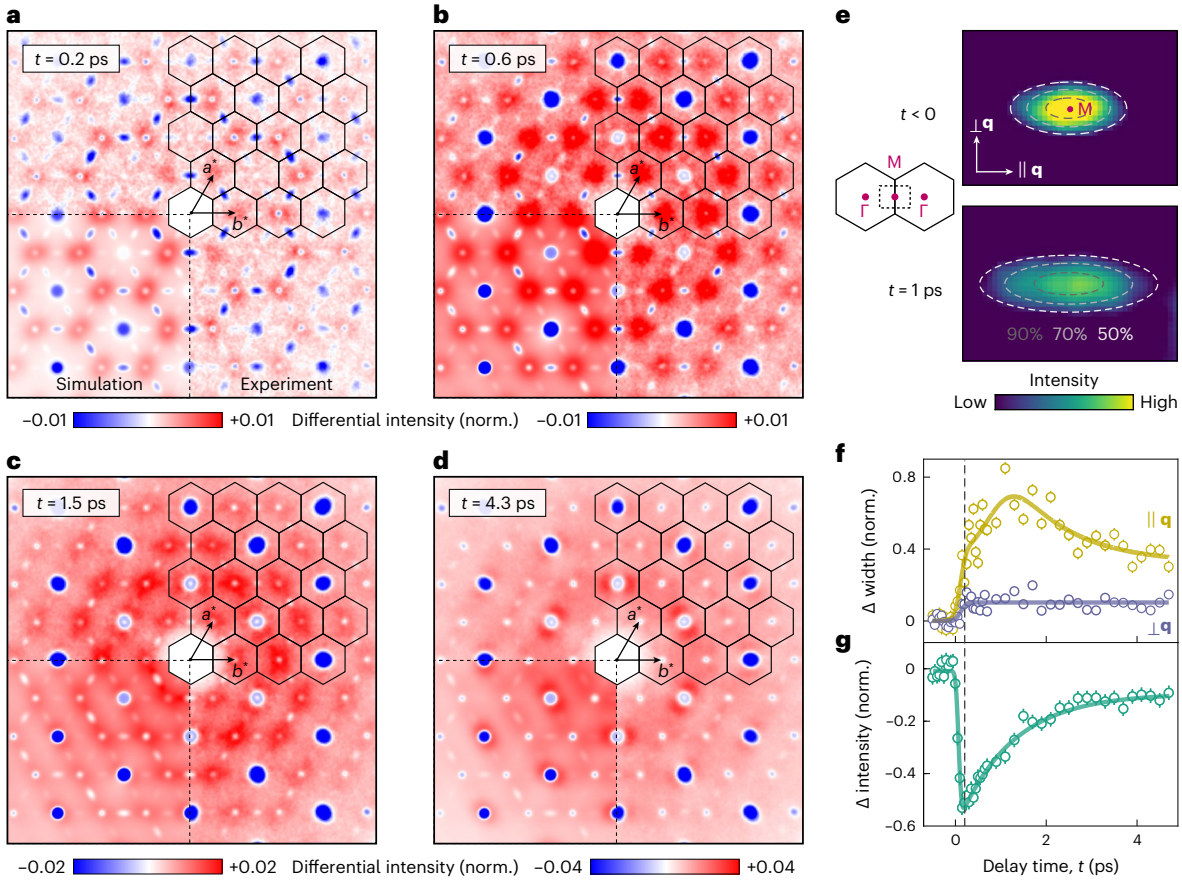

Fig. 2 | Photoinduced 1D domain walls in the CDW. a–d, Differential electron diffraction intensity at four time delays after photoexcitation by a 3 mJ cm^{-2}, 800 nm pulse; data were taken at 210 K. The lower-left quadrant shows the simulation result (Supplementary Note 5). Intensity changes are normalized by the pre-excitation values; note the different colour scales in different panels. The hexagons mark the Brillouin zones and images are symmetrized to enhance statistics. The white centre of the {110} peaks is due to detector saturation in the centre of these brightest Bragg peaks; therefore, the intensity difference is zero (that is, white colour). Supplementary Fig. 3a–e shows the equilibrium diffraction and unsymmetrized patterns, and Supplementary Video 1 shows the continuous evolution of diffraction intensity. **e**, Comparison of the 2D CDW peak at the M point before and 1 ps after photoexcitation, where signals from multiple M points that are symmetry-equivalent to $(H, K) = (3.0, -1.5)$ are averaged. The dashed rectangle in the inset marks the bounding box of the images. The dashed ellipses are fitted intensity contours at different levels relative to the peak intensity. **f**, Time evolution of the change in peak width at M. Much more broadening is observed in the direction parallel to the CDW wavevector ($\parallel\mathbf{q}$) than the perpendicular direction ($\perp\mathbf{q}$). **g**, Time evolution of the change in peak intensity at M. The vertical dashed line marks the minimum of the transient intensity. In **f** and **g**, all the quantities are normalized to their respective values before pump incidence; the error bars represent the standard deviation of their pre-excitation values. The solid curves are fits to Supplementary Equation (6) (blue curve), Supplementary Equation (7) (green curve) and their sum (yellow curve). Supplementary Note 8 provides the curve-fitting details.

an isotropic peak broadening points to the formation of dislocations (Fig. 1g) (Supplementary Note 2). If this broadening is predominantly perpendicular to $\mathbf{q}_1$, coherence between neighbouring displacement chains is maintained but reduced along the chain direction, consistent with shear (Fig. 1f). On the other hand, peak broadening parallel to $\mathbf{q}_1$ signifies the appearance of one-dimensional (1D) domain walls, which consist of adjacent chains with in-phase atomic displacements (Fig. 1e). In all these cases, the CDW defects are topological and they can only be created or annihilated in defect–anti-defect pairs[20].

The experiments were carried out on a freestanding thin flake of 1T-$TiSe_2$ at 210 K in its 2D CDW state (Methods). Following photoexcitation by a 3 mJ cm^{-2}, 800 nm pulse, the change in diffraction pattern recorded with MeV relativistic electrons is shown in Fig. 2a–d along the [001] zone axis; Supplementary Video 1 shows the continuous evolution of diffraction intensity. Owing to the high electron energy, these differential maps reveal a rich set of diffuse patterns with a wide momentum range that are less affected by dynamical scattering effects compared with kiloelectronvolt electrons[25], yielding critical information about the microscopic environment surrounding the creation of CDW defects.

We first focus on photoinduced changes near the M point that report the 2D CDW dynamics. The emergence of blue spots in the difference map (Fig. 2a) indicates a transient suppression of the CDW amplitude[24,26]. Their elongated shape with the long axis oriented perpendicular to the Brillouin-zone boundary further suggests anisotropic peak broadening. In Fig. 2e, we zoom into a particular M point corresponding to one of the three CDW wavevectors, and we examine the diffuse intensity profile before and 1 ps after photoexcitation. As illustrated in the fitted contours (dashed ellipses), the peak width increases substantially in the direction parallel to the CDW wavevector ($\parallel\mathbf{q}$), whereas much smaller broadening occurs in the perpendicular direction ($\perp\mathbf{q}$). As the CDW correlation length is inversely proportional to the peak width, we estimate the correlation length to be 5.3 unit cells (defined in the non-CDW state) parallel to $\mathbf{q}$ and 17.3 unit cells perpendicular to $\mathbf{q}$ at 1 ps (Supplementary Note 3). Based on the schematic shown in Fig. 1e, the anisotropic peak broadening suggests that photoexcitation gives rise to 1D domain walls, which constitute the most probable atomic arrangement despite the lack of a probe to image these defects in real space; additional analysis of the diffraction patterns shows that other effects, such as photoinduced strain, can

https://doi.org/10.1038/s41567-023-02279-x

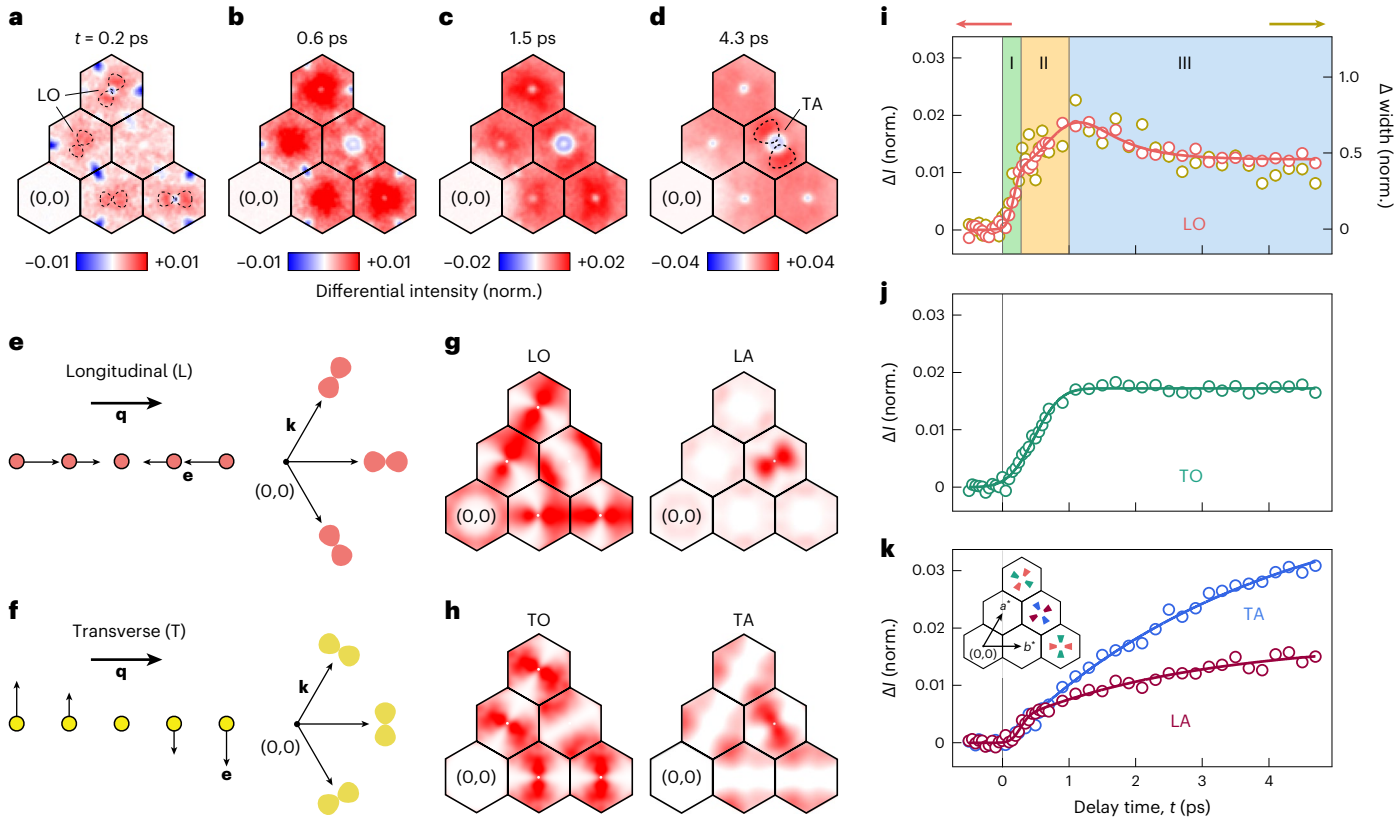

Fig. 3 | Photoinduced phonon dynamics in different branches. **a**–**d**, Differential diffraction patterns taken from Fig. 2a–d, zooming into the six Brillouin zones near the undiffracted beam at (0, 0). Regions of interest marked by the dashed curves in **a** and **d** highlight the diffuse scatterings from LO phonons and TA phonons, respectively. **e**,**f**, Schematic of the atomic displacements (left) and diffuse scatterings (right) for longitudinal (**e**) and transverse (**f**) phonons for a given wavevector **q**, which is defined from the closest Γ point. The scattering wavevector **k** is measured with respect to (0, 0). **g**,**h**, Calculated one-phonon structure factor for longitudinal (L) and transverse (T) phonons from the optical (O) and acoustic (A) branches. The structure factor of optical phonons concentrates in Brillouin zones with $(H - K) \neq 0 \pmod 3$; the opposite holds true for acoustic phonons. Supplementary Figs. 6 and 7 show the full images with more Brillouin zones included. **i**–**k**, Time evolution of diffuse intensities for different phonon branches, taken from colour-coded regions of interests (**k**, inset). Intensities from symmetry-equivalent Brillouin zones are averaged. The solid curves are fits to Supplementary Equation (6) (TO), Supplementary Equation (7) (TA and LA) and their sum (LO). In **i**, the time trace of the 2D CDW peak width parallel to the CDW wavevector is overlaid (yellow circles, reproduced from Fig. 2f). Both width and LO phonon population show similar three-part dynamics (labelled I–III), which are qualitatively distinct from TO, TA and LA phonons in **j** and **k**.

be excluded (Supplementary Note 4 provides a detailed discussion of alternative scenarios). To further confirm our defect assignment, we simulated the change in M-point intensity using anisotropic CDW correlations for all three wavevectors (Supplementary Note 5). The computed patterns (Fig. 2a–d, bottom left) demonstrate an excellent agreement with the experimental data.

These chain-like domain walls distinguish 1T-$TiSe_2$ from previous experimental and theoretical studies of transient defects in CDW compounds where dislocation pairs are created by photoexcitation[7,8,27,28]. Here the preferential formation of 1D domain walls instead of point-like dislocations validates an early prediction that CDWs in 1T-$TiSe_2$ can be viewed as weakly linked chains[29], which are further evidenced by similar anisotropy observed in photoinduced peak broadening below T_c (Supplementary Note 6). From the theoretical standpoint, both second-order Jahn–Teller distortion and excitonic interaction between Se 4*p* holes and Ti 3*d* electrons are thought to account for the underlying 1D nature of the CDW in equilibrium. In our experiments, the high photoexcitation density leads to the generation of free carriers that transiently screen excitonic correlations, which remain suppressed as the 1D domain walls grow[30]. Hence, excitons are not expected to play an important role in maintaining this 1D-chain configuration in the non-equilibrium context.

To understand how the 1D domain walls are created in the 2D CDW, we plot the M-point peak widths in two orthogonal directions as a function of pump–probe delay (Fig. 2f). For comparison, we also show the time evolution of the peak intensity (Fig. 2g), which reports the local amplitude of the order parameter[31]. Within 200 fs after photoexcitation, the CDW amplitude reaches a minimum (Fig. 2f,g, vertical dashed line). A similar timescale (200–300 fs) marks the initial peak broadening in both directions: parallel (yellow circles) and perpendicular (blue circles) to the CDW wavevector **q**. After 300 fs, the CDW amplitude starts to recover and the peak width perpendicular to **q** remains constant. On the other hand, the peak width parallel to **q** continues to grow up to ~1 ps, leading to an increasingly more anisotropic peak. The observation that anisotropic broadening lasts beyond the initial intensity suppression allows us to divide the domain wall formation into two stages. First, the transient loss of local CDW amplitude triggers a concurrent suppression of CDW coherence, suggesting that the atomic displacement towards the high-symmetry position is not executed in a concerted manner[32]. In particular, although displacements within a CDW chain are largely coherent, substantial disordering occurs between different CDW chains, leading to domain wall formation. In the second stage, further development of chain-like domain walls relies on a partial CDW amplitude recovery, where adjacent chains adopt an in-phase instead of anti-phase displacement as atoms move back to the distorted lattice positions, akin to a local CDW phase inversion[3,33]. Beyond ~1 ps, domain walls start the slow annihilation

https://doi.org/10.1038/s41567-023-02279-x

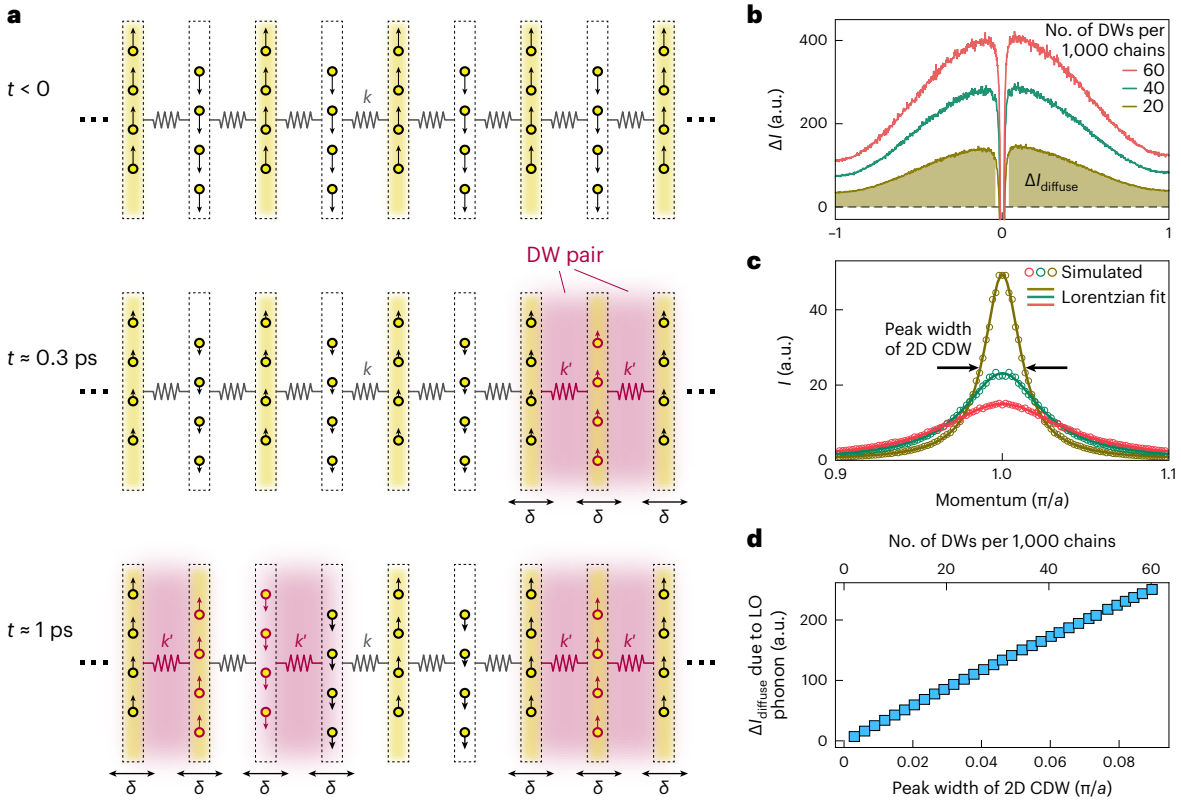

Fig. 4 | Ultrafast domain wall creation mediated by LO phonons. a, Schematic of the dual-stage formation of CDW domain walls (DWs) illustrated for a particular CDW wavevector. Only Ti atoms are shown (circles), where arrows denote CDW displacements. In the first stage (up to ~0.3 ps), the CDW amplitude decreases, represented by the shrinking arrow length; in the second stage (up to ~1 ps), the CDW amplitude partially recovers. Pairs of DWs are indicated by the red shade, where CDW displacements in the opposite direction compared with the $t < 0$ configuration are highlighted by the red arrows. DW formation modifies the local interchain coupling ($k \rightarrow k'$), leading to local displacements (δ) that constitute the LO phonons. **b**, Simulated change in diffuse scattering intensity due to longitudinal phonons arising from local atomic displacements at DWs (δ motion in **a**). The simulations were performed for a variable number of DW densities. The dip at zero momentum (Γ point) reflects the Debye–Waller intensity drop of the Bragg peak. The shaded area represents the momentum range for calculating the integrated intensity $\Delta I_{\mathrm{diffuse}}$ used in **d**. **c**, Simulated CDW peak at the Brillouin-zone boundary for various DW densities (same colour coding as **b**). The solid curves are Lorentzian fits. **d**, Simulated diffuse intensity change arising from LO phonons as a function of CDW DW densities (top axis), or equivalently, the width of the 2D CDW peak (bottom axis). a.u., arbitrary units.

process, and the change in the M-point peak width remains highly anisotropic throughout our time window up to 4.7 ps. These observations were reproduced in different samples, and the defect formation dynamics were found to be independent of pump-laser polarization (Supplementary Note 7).

Although we have identified two stages of defect formation that are demarcated by the transient minimum of the CDW amplitude, it remains elusive what microscopic process contributes to phase disordering between adjacent chains during either stage. As domain wall formation fundamentally represents a special type of lattice dynamics, we look into non-thermal phonon populations induced by the femtosecond laser pulse, whose evolution is encoded in diffuse scattering signals away from Bragg peaks (Γ point) and 2D CDW peaks (M point). In Fig. 3a–d, we re-examine the differential intensity patterns, zooming into the six Brillouin zones closest to the (0, 0) order. Based on the momentum anisotropy of red diffuse features, we can categorize them into either longitudinal or transverse phonons (Fig. 3e,f). For example, at 0.2 ps, elongated diffuse signals resembling an hourglass shape are observed near the Brillouin-zone centres (Fig. 3a, dashed curves), where the elongation is parallel to the line connecting the zone centre (Γ point) and (0, 0). These are primarily longitudinal phonons, whose polarization vector **e** is parallel to the phonon wavevector **q** defined relative to the Γ point. This assignment originates from the fact that the one-phonon structure factor contains a term $(\mathbf{e} \cdot \mathbf{k})$, where **k** is the scattering wavevector measured from (0, 0) (ref. 34). Hence, the most prominent diffuse intensity appears in regions of the Brillouin zone where $\mathbf{q} \| \mathbf{k}$. The same argument implies that transverse phonons near the Γ point appear in similarly shaped diffuse features but are 90° rotated (Fig. 3f). This is the case at 4.3 ps in the (1, 1) Brillouin zone (Fig. 3d, dashed curves). Using phonon structure factors obtained from first-principles calculations, we can further break down longitudinal and transverse phonons into optical and acoustic branches (Supplementary Note 5). Specifically, diffuse signals from optical phonons are more intense in (H, K) zones where $(H - K) \neq 0 \pmod 3$; the opposite applies to acoustic phonons (Fig. 3g,h). Hence, at 0.2 ps, the longitudinal optical (LO) phonons are the first to be excited among all branches (Fig. 3a), whereas the quasi-equilibrium state at 4.3 ps is characterized by a dominant population of transverse acoustic (TA) phonons (Fig. 3d). These assignments are further confirmed by diffuse scattering simulations (Fig. 2a–d, bottom left), which accurately reproduce the experimental observation, including the suppression of Bragg peaks at long time delay primarily due to the acoustic phonons emitted.

To quantify the non-thermal phonon population, we plot the diffuse intensity evolution (Fig. 3i–k) for the four types of phonons: LO, transverse optical (TO), longitudinal acoustic (LA) and TA. Below 300 fs, the LO phonons are preferentially excited, which continue to grow after 300 fs but at a smaller rate of increase (Fig. 3i). Their population subsequently decreases after 1 ps and reaches a metastable value. This three-part evolution of the LO phonons (labelled I–III in Fig. 3i) distinguishes them from TO, TA and LA phonons, which mainly feature

a rise on slower timescales without any relaxation over a few picoseconds (Fig. 3j,k; Supplementary Note 8 provides further analyses of the evolution of the phonon populations). In particular, the LO phonon dynamics (Fig. 3i, red circles) almost exactly coincide with the change in CDW peak width in the direction parallel to the CDW wavevector (Fig. 3i, yellow circles), both showing a dual-stage growth followed by relaxation (Supplementary Fig. 14 and Supplementary Table 1 provide a quantitative comparison). As the peak width scales with the domain wall density, this correlation suggests that the emission of LO phonons from excited electrons plays a critical role in creating the topological defects in the 2D CDW.

We can gain some insight into the coupling between LO phonons and 1D domain walls by considering the model of linked CDW chains for each of the three CDW wavevectors[29] (Supplementary Note 9 provides the modelling details). Here we treat each chain as an individual entity coupled by a spring constant k, where LO phonons manifest as local, non-propagating oscillations that modulate the interchain distance (Fig. 4a). The most drastic change in the interchain coupling is expected to occur at CDW domain walls due to the in-phase atomic displacements in two neighbouring chains (Fig. 4a, red-shaded regions). This modification of the spring constant from k to k' inevitably leads to a change in the local interchain distance and hence the excitation of LO phonons at the domain wall (δ vibrations; Fig. 4a). Conversely, the non-thermal population of LO phonons can result in large interchain displacements, where in-phase rather than out-of-phase CDW distortions can be locally favoured, seeding the growth of a domain wall. To be more quantitative, from this model, we compute the change in diffuse intensity associated with LO phonons ($\Delta I_{\mathrm{diffuse}}$; Fig. 4b) for various domain wall densities, which are proportional to the peak widths of the 2D CDW in the direction parallel to the CDW wavevector (Fig. 4c). The nearly perfect linear relation between $\Delta I_{\mathrm{diffuse}}$ and peak width (Fig. 4d) provides a natural explanation for their overlapping temporal evolutions observed in Fig. 3i. Our calculation further predicts that the momentum-space profile of the phonon diffuse signal remains unaltered despite a change in intensity (Supplementary Fig. 15e). This universal line profile is clearly evidenced in the experimental diffraction pattern (Supplementary Fig. 15d), lending further support to our model.

The simultaneous measurements of both 2D CDW peaks and diffuse phonon signals offer a detailed picture of how topological defects develop in two stages in the sub-picosecond regime (Fig. 4a). Approximately within the first 300 fs—a timescale not limited by the temporal resolution of the instrument (Supplementary Note 1)—a high density of free carriers excited by the laser pulse transiently suppress the CDW amplitude. At the same time, a rapidly increasing LO phonon population substantially modulates the interchain interaction, leading to predominantly local flips of the CDW displacement direction and the production of pairs of 1D domain walls. During the second stage that lasts up to 1 ps, the CDW amplitude starts to recover, but continued emission of the LO phonons creates local minima in the energy landscape where in-phase CDW displacements between neighbouring chains are preferred. Hence, more pairs of domain walls are formed, which are not annihilated until several picoseconds or longer. The rate of domain wall growth is markedly higher during the first stage than the second stage (Fig. 2f), a consequence of the lower energy cost of domain walls when the local CDW amplitude is being suppressed.

The 1D domain walls identified in this study disrupt the translational order of the 2×2 CDW in 1T-$TiSe_2$ and respect the three-fold rotational symmetry. The resulting state is consistent with hexatic order that appears as an intermediate phase when a 2D triangular lattice is melted by the dissociation of bound topological defects[15]. Our work provides the missing time axis in the sub-picosecond scale for describing this defect-driven transition, highlighting the role of longitudinal phonons in mediating domain wall generation. We expect the mechanism discovered here to be general for other broken-symmetry states characterized by a complex order parameter, where defect generation takes place regardless of the amplitude of the order parameter but is, instead, associated with the non-thermal excitation of collective modes like the longitudinal phonons in this study. Our result paves the way for the ultrafast manipulation of topological defects in different broken-symmetry phases, a fruitful avenue for discovering emergent orders in correlated materials[35].

Online content

Any methods, additional references, Nature Portfolio reporting summaries, source data, extended data, supplementary information, acknowledgements, peer review information; details of author contributions and competing interests; and statements of data and code availability are available at https://doi.org/10.1038/s41567-023-02279-x.

References

1. Yusupov, R. et al. Coherent dynamics of macroscopic electronic order through a symmetry breaking transition. *Nat. Phys.* **6**, 681–684 (2010).
2. Zong, A. et al. Ultrafast manipulation of mirror domain walls in a charge density wave. *Sci. Adv.* **4**, eaau5501 (2018).
3. Duan, S. et al. Optical manipulation of electronic dimensionality in a quantum material. *Nature* **595**, 239–244 (2021).
4. Stojchevska, L. et al. Ultrafast switching to a stable hidden quantum state in an electronic crystal. *Science* **344**, 177–180 (2014).
5. Gerasimenko, Y. A., Karpov, P., Vaskivskyi, I., Brazovskii, S. & Mihailovic, D. Intertwined chiral charge orders and topological stabilization of the light-induced state of a prototypical transition metal dichalcogenide. *npj Quantum Mater.* **4**, 32 (2019).
6. Kogar, A. et al. Light-induced charge density wave in $LaTe_3$. *Nat. Phys.* **16**, 159–163 (2020).
7. Vogelgesang, S. et al. Phase ordering of charge density waves traced by ultrafast low-energy electron diffraction. *Nat. Phys.* **14**, 184–190 (2018).
8. Zong, A. et al. Evidence for topological defects in a photoinduced phase transition. *Nat. Phys.* **15**, 27–31 (2019).
9. Laulhé, C. et al. Ultrafast formation of a charge density wave state in 1T-TaS_2: observation at nanometer scales using time-resolved X-ray diffraction. *Phys. Rev. Lett.* **118**, 247401 (2017).
10. Chuang, I., Durrer, R., Turok, N. & Yurke, B. Cosmology in the laboratory: defect dynamics in liquid crystals. *Science* **251**, 1336–1342 (1991).
11. Bowick, M. J., Chandar, L., Schiff, E. A. & Srivastava, A. M. The cosmological Kibble mechanism in the laboratory: string formation in liquid crystals. *Science* **263**, 943–945 (1994).
12. Orihara, H. & Ishibashi, Y. Dynamics of disclinations in twisted nematics quenched below the clearing point. *J. Phys. Soc. Jpn* **55**, 2151–2156 (1986).
13. Nagaya, T., Hotta, H. & Oriharaand Yoshihiro Ishibashi, H. Experimental study of the coarsening dynamics of +1 and −1 disclinations. *J. Phys. Soc. Jpn* **61**, 3511–3517 (1992).
14. Nakai, A., Shiwaku, T., Wang, W., Hasegawa, H. & Hashimoto, T. Phase-separated structures formed in polymer mixtures containing a thermotropic liquid crystalline copolyester as one component. *Polymer* **37**, 2259–2272 (1996).
15. Nelson, D. R. & Halperin, B. I. Dislocation-mediated melting in two dimensions. *Phys. Rev. B* **19**, 2457–2484 (1979).
16. Dai, H., Chen, H. & Lieber, C. M. Weak pinning and hexatic order in a doped two-dimensional charge-density-wave system. *Phys. Rev. Lett.* **66**, 3183–3186 (1991).
17. Soumyanarayanan, A. et al. Quantum phase transition from triangular to stripe charge order in $NbSe_2$. *Proc. Natl Acad. Sci. USA* **110**, 1623–1627 (2013).
18. Ma, L. et al. A metallic mosaic phase and the origin of Mott-insulating state in 1T-TaS_2. *Nat. Commun.* **7**, 10956 (2016).

19. Cho, D. et al. Nanoscale manipulation of the Mott insulating state coupled to charge order in 1T-TaS_2. *Nat. Commun.* **7**, 10453 (2016).
20. Chaikin, P. M. & Lubensky, T. C. *Principles of Condensed Matter Physics* (Cambridge Univ. Press, 1995).
21. Qi, F. et al. Breaking 50 femtosecond resolution barrier in MeV ultrafast electron diffraction with a double bend achromat compressor. *Phys. Rev. Lett.* **124**, 134803 (2020).
22. Stern, M. J. et al. Mapping momentum-dependent electron-phonon coupling and nonequilibrium phonon dynamics with ultrafast electron diffuse scattering. *Phys. Rev. B* **97**, 165416 (2018).
23. Chen, P. et al. Hidden order and dimensional crossover of the charge density waves in $TiSe_2$. *Sci. Rep.* **6**, 37910 (2016).
24. Cheng, Y. et al. Light-induced dimension crossover dictated by excitonic correlations. *Nat. Commun.* **13**, 963 (2022).
25. Zhu, P. et al. Femtosecond time-resolved MeV electron diffraction. *New J. Phys.* **17**, 063004 (2015).
26. Otto, M. R. et al. Mechanisms of electron-phonon coupling unraveled in momentum and time: the case of soft phonons in $TiSe_2$. *Sci. Adv.* **7**, eabf2810 (2021).
27. Domröse, T. et al. Light-induced hexatic state in a layered quantum material. *Nat. Mater*. https://doi.org/10.1038/s41563-023-01600-6 (2023).
28. Tarkhov, A. E., Rozhkov, A. V. & Fine, B. V. Dynamics of topological defects after photoinduced melting of a charge density wave. *Phys. Rev. B* **106**, L121109 (2022).
29. van Wezel, J., Nahai-Williamson, P. & Saxena, S. S. Exciton-phonon-driven charge density wave in $TiSe_2$. *Phys. Rev. B* **81**, 165109 (2010).
30. Porer, M. et al. Non-thermal separation of electronic and structural orders in a persisting charge density wave. *Nat. Mater.* **13**, 857–861 (2014).
31. Zong, A. et al. Role of equilibrium fluctuations in light-induced order. *Phys. Rev. Lett.* **127**, 227401 (2021).
32. Wall, S. et al. Ultrafast disordering of vanadium dimers in photoexcited VO_2. *Science* **362**, 572–576 (2018).
33. Zhang, Y. et al. Creation of a novel inverted charge density wave state. *Struct. Dyn.* **9**, 014501 (2022).
34. Xu, R. & Chiang, T. C. Determination of phonon dispersion relations by X-ray thermal diffuse scattering. *Z. Krist. Cryst. Mater.* **220**, 1009–1016 (2005).
35. de la Torre, A. et al. Colloquium: nonthermal pathways to ultrafast control in quantum materials. *Rev. Mod. Phys.* **93**, 041002 (2021).

Methods

Sample growth and preparation

High-quality single crystals of 1T-$TiSe_2$ were grown by chemical vapour transport with an iodine transport agent. Ti and Se were mixed in a molar ratio of 1:2 and placed into an alumina crucible before being sealed into a quartz tube. The quartz tube was heated to 700 °C and 1T-$TiSe_2$ crystals were synthesized at the 650 °C zone for two weeks. The 1T-$TiSe_2$ thin flakes were obtained by the repeated exfoliation of the bulk crystal with polydimethylsiloxane films (Gel-Pak). Flakes were pre-screened for thickness and uniformity with an optical microscope using the colour contrast and further characterized by atomic force microscopy. Selected flakes were detached from polydimethylsiloxane in ethanol and scooped onto standard copper transmission electron microscopy grids. The resulting freestanding flake has a typical lateral dimension of ~400 μm and thickness of ~30 nm. Supplementary Note 10 provides an optical image and temperature-dependent equilibrium diffraction characterization of a typical flake.

MeV ultrafast electron diffraction

Details of the ultrafast electron diffraction beamline are discussed elsewhere[21]. Briefly, the 800 nm (1.55 eV), 30 fs pulses from a Ti:sapphire regenerative amplifier system operating at a repetition rate of 100 Hz (Vitara and Legend Elite Duo HE, Coherent) were split into pump and probe branches. The probe branch was frequency tripled in nonlinear crystals before illuminating a photocathode for electron-pulse generation, producing approximately 30,000 electrons per pulse (5 fC). After being accelerated by an intense radio-frequency field to relativistic velocity (~0.989c), the electron beam went through a double-bend achromatic lens for pulse compression and jitter removal. The typical electron-beam spot size on the sample was approximately 150 μm measured at a full-width at half-maximum. This size was nearly five times smaller than the size of the pump pulse, ensuring a homogeneous photoexcitation condition. The temporal delay between the pump and probe pulses was adjusted by a linear translation stage, and the temporal resolution was 58 fs measured at the full-width at half-maximum (Supplementary Note 1 provides a detailed characterization of time resolution). Diffracted electron beams were incident on a phosphor screen (P43) and the image was collected by an electron-multiplying charge-coupled device. The sample was cooled by liquid nitrogen.

Data availability

All data supporting the conclusions are available within the article and its Supplementary Information. Additional data are available from the corresponding authors upon reasonable request.

Acknowledgements

We thank Y. He and D. Limmer for helpful discussions. We thank J.-H. Pöhls for providing the calculated phonon dispersions[26] and L. P. René de Cotret for providing the Python codes for computing the one-phonon structure factor[22]. D.X. and J.Z. acknowledge support from the National Key R&D Program of China (no. 2021YFA1400202); the National Natural Science Foundation of China (grant nos. 11925505, 11504232 and 11721091); and the Office of Science and Technology, Shanghai Municipal Government (no. 16DZ2260200). A.Z. acknowledges support from the Miller Institute for Basic Research in Science. L.W., Q.M. and Y.Z. acknowledge support from the US Department of Energy, Basic Energy Sciences, Materials Sciences and Engineering Division, under Contract No. DE-SC0012704. Y.G. acknowledges support from the National Natural Science Foundation of China (grant no. 11874264). A.K. acknowledges support from the US Department of Energy (DOE), Office of Science, Office of Basic Energy Sciences under Award No. DE-SC0023017. M.W.Z. acknowledges funding by the W. M. Keck Foundation, funding from the UC Office of the President within the Multicampus Research Programs and Initiatives (M21PL3263), the Hellman Fellows Fund and the National Science Foundation (NSF-DMR 2247363).

Author contributions

A.Z., D.X. and Y.C. conceived the project. Y.C., A.Z., L.W. and Y.Z. analysed the data with important theoretical insights from J.v.W. and A.K. W.X. and Y.G. grew the single crystals. Y.C. collected the ultrafast electron diffraction data, where the MeV ultrafast electron diffraction beamline was constructed and maintained by F.Q., P.Z., X.Z. and T.J. L.W., Q.M. and Y.C. performed the diffraction simulations. A.Z. and Y.C. wrote the paper with critical input from A.K., M.W.Z., Y.Z., D.X. and all other authors. The project was supervised by M.W.Z., J.Z., Y.Z. and D.X.

Competing interests

The authors declare no competing interests.

Additional information

Supplementary information The online version contains supplementary material available at https://doi.org/10.1038/s41567-023-02279-x.

Correspondence and requests for materials should be addressed to Alfred Zong, Michael W. Zuerch, Jie Zhang, Yimei Zhu or Dao Xiang.

Peer review information *Nature Physics* thanks Isabella Gierz, Dragan Mihailović and the other, anonymous, reviewer(s) for their contribution to the peer review of this work.